We are IntechOpen, the world's leading publisher of Open Access books Built by scientists, for scientists

5,300
Open access books available

130,000
International authors and editors

155M
Downloads

Our authors are among the

154
Countries delivered to

TOP 1%
most cited scientists

12.2%
Contributors from top 500 universities

CLARIVATE ANALYTICS BOOK CITATION INDEX INDEXED

WEB OF SCIENCE™

Selection of our books indexed in the Book Citation Index in Web of Science™ Core Collection (BKCI)

Interested in publishing with us?
Contact book.department@intechopen.com

Numbers displayed above are based on latest data collected.
For more information visit www.intechopen.com

Chapter 8

Plasmonic Lenses

Yongqi Fu, Jun Wang and Daohua Zhang

Additional information is available at the end of the chapter

http://dx.doi.org/10.5772/50029

1. Introduction

The resolution of almost all conventional optical system is indispensably governed by the diffraction limit. This resolution limit can be overcome by use of focusing the evanescent waves in the near field region. The concept of "superlens" was proposed firstly by Pendry in 2000 [1]. When ε= -1and μ= -1, the negative refractive index material plate can be a perfect lens [2-4]. Because of the dispersion and absorption in the materials, the conditions of ε= -1and μ= -1 is hard to satisfy for the natural materials. Although the perfect lens may not exist, the superlens which can provide higher resolution beyond the diffraction limit have been proved. And focusing by means of surface plasmon polarisons (SPPs) by plasmonic lens is attracting much interest recently due to its unique feature of extraordinary enhanced transmission [5-8]. It means that we can focus the evanescent components of an illuminated object in the near-field region with subdiffraction-limit resolution [9]. This allows them to break the conventional barrier of diffraction limit, and leads to the formation of concentrated sub-wavelength light spots on the order of nanometers. Plasmonic lens is always consisted by metal and dielectric and can excite SPPs and always can be used for focusing, imaging, and beam shaping and so on.

In this paper, a literature review is given for the purpose of displaying a physical picture of plasmonic lenses for the relevant reader. Firstly, the basic theory about the plasmonic lens is presented. Then several examples of plasmonic lens are given. Here we mainly focus on the typical concepts of the plasmonic lens reported so far.

2. Plasmonic lens on the basis of negative refractive index materials

2.1. Superlens

Although perfect lens proposed by Pendry may not exist, superlens is realized and proved by Zhang's group in 2003 [10-13] and other research groups [14-21]. Here we mainly introduce the typical works which were done by Zhang's group. They showed that optical

evanescent waves could indeed be enhanced as they passed through a sliver superlens. Figure 1 below shows configuration of the superlens they designed.

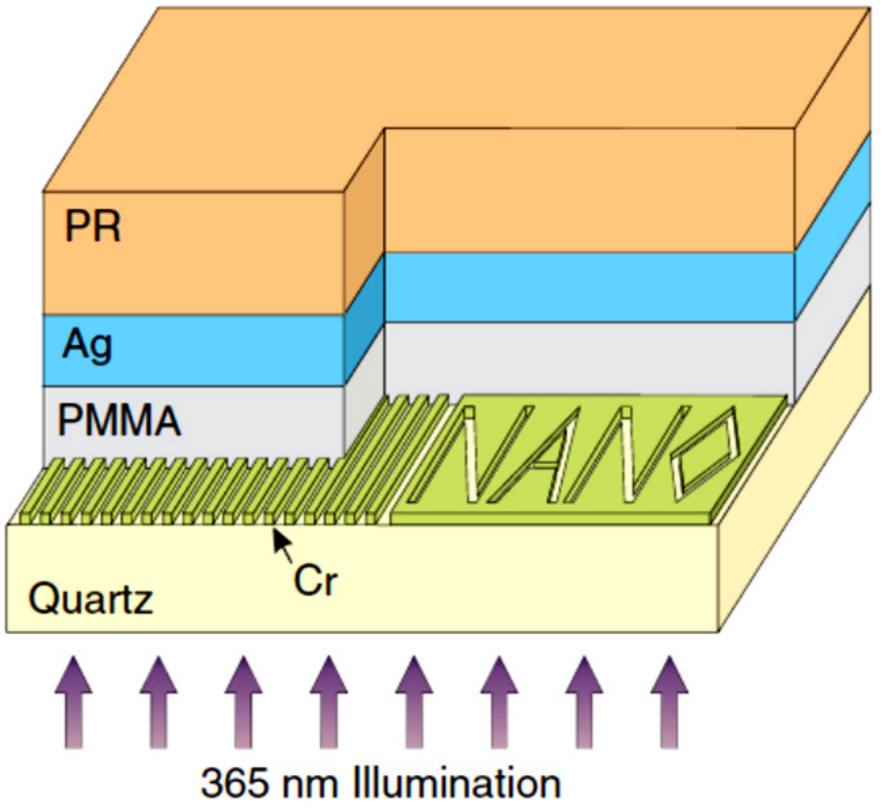

Figure 1. Optical superlensing designed by Zhang's group. Reprinted with permission from "N. Fang, H. Lee, C. Sun and X. Zhang, Science 308, 534-537 (2005)." of copyright ©2005 American Institute of Physics.

As can be seen, a set of objects were inscribed onto a chrome screen. The objects were designed to be placed about 40 nm away from the silver film which is 35 nm in thickness. And the chrome objects were patterned on quartz by using focused ion beam (FIB) technique, a 40 nm thick layer of polymethyl methacrylate (PMMA) was used to planarized them. The objects are imaged onto the photoresist on the other side of the silver film under ultraviolet (UV) illumination (at a wavelength of 365 nm). The negative photoresist which is 120 nm thick is used to record the near-field image. The substrate is food-exposed under an I-line (365 nm) mercury lamp. The exposure flux is 8 mW/cm^2, and an optimal exposure time of 60 s is applied to reduce the surface root mean square modulation below 1 nm for both the silver and PMMA surfaced; otherwise, the dispersion characteristics of the superlens would be modified and would in turn smear the details of the recorded image. The optical image is converted into topographic modulations by developing the negative photoresist and is mapped using atomic force microscopy (AFM).

Because the electric and magnetic responses of materials were decoupled in the near field, only the permittivity needs to be considered for transverse magnetic (TM) waves. This makes noble metals such as silver natural candidates for optical superlensing. Silver is chosen here. As surface charges accumulate at the interface between the silver and the imaging medium, the normal component of an electric of silver is selected and the permittivity of the silver and

that of the adjacent medium are equal and of opposite sign. Such a delicate resance is essential to ensure the evanescent enhancement across the slab. For enhanced transmission of evanescent waves, it is found that an asymptotic impedance match ($k_{zi} / \varepsilon_i + k_{zj} / \varepsilon_j = 0$) has to be met at the surface of the silver, known as the surface plasmon excitation condition (k_{zi}, cross-plane, wave vector in silver; ε_i, permittivity of silver; k_{zj}, cross-plane wave vector in dielectric; and ε_j, permittivity of dielectric). It is widely known in metal optics that when the two media take the opposite sign in permittivity and $|\varepsilon_i| >> \varepsilon_j$, only surface plasmons at the narrow range of in-plane wave vector (k_x) that are close to ko can be resonantly coupled. However, less well known is that when $|\varepsilon_i| \sim \varepsilon_j$ and we are of opposite sign, the excitable surface plasmon band of k_x is significantly broadened, resulting in the superlensing effect.

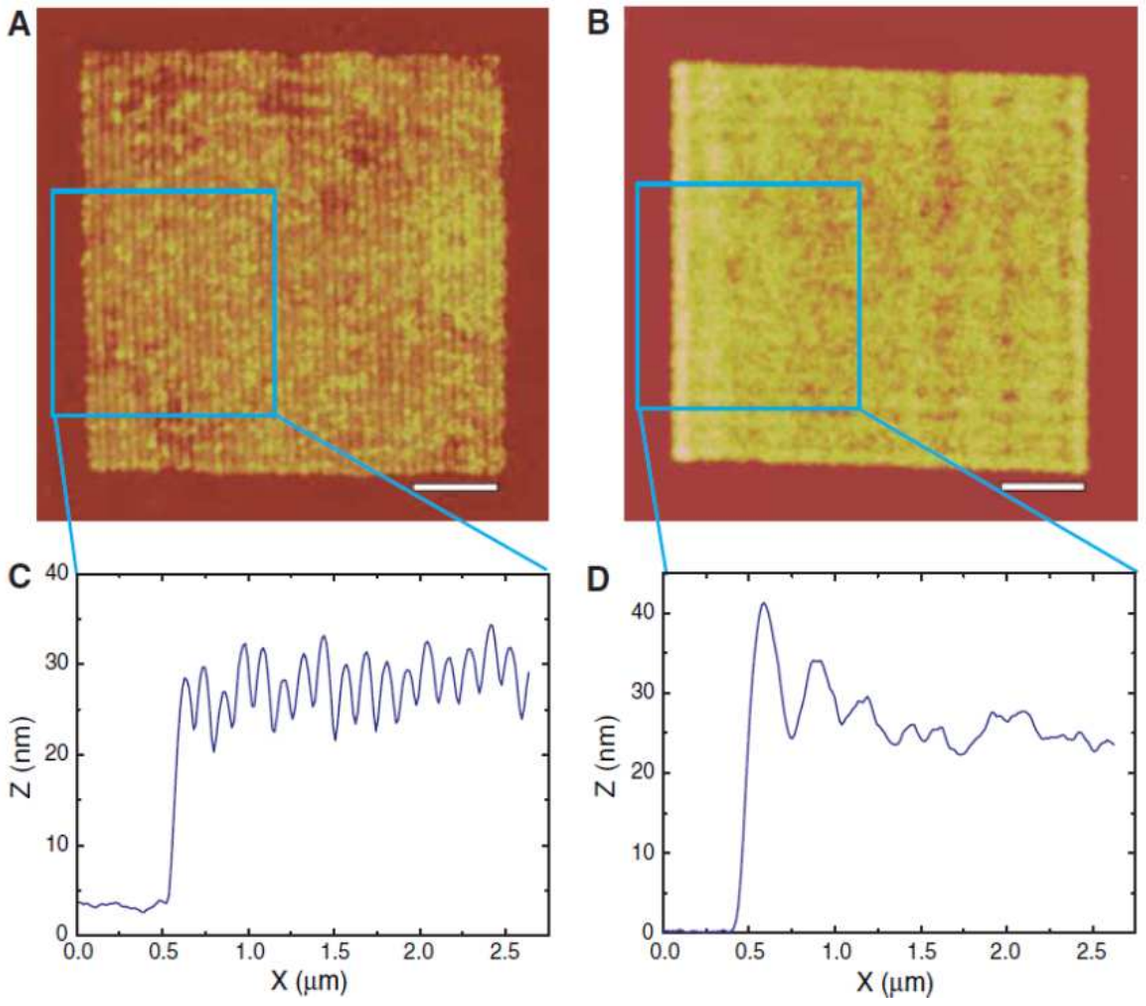

Figure 2. (A) AFM of the developed image (scale bar, 1 μm; color scale from dark red to bright yellow, 0 to 150 nm). (B) Control experiments were carried out, in which the silver superlens layer was replaced by a 35 nm thick PMMA layer, for a total PMMA thickness of 75nm. (C) The blue solid curve shows the clearly demonstrating the 63 ± 4 nm half-pitch resolved with a 35 nm silver superlens. X direction is relative displacement along the cross-section direction. (D) The blue solid curve shows the average cross section of Fig. 2B (control sample). Reprinted with permission from "N. Fang, H. Lee, C. Sun and X. Zhang, Science 308, 534-537 (2005)." of copyright ©2005 American Institute of Physics.

The intensity of evanescent waves decays with a characteristic length Z, and

$$Z^{-1} = 4\pi\sqrt{a^{-2} - \varepsilon\lambda^{-2}}\ , \tag{1}$$

where a is the period of a line array, and ε is the permittivity of the surrounding media. In Zhang's experiment, for the 60 nm half-pitch and ε = 2.4, the decay length is estimated to be 11 nm. Thus it is obviously difficult to resolve a 60 nm half-pitch object from a distance of 75 nm away if there isn't a superlens to enhance and transmit the evanescent waves. So we could find the photoresist images with typical average height modulations of 5 nm to 10 nm from Fig. 2 C. And this is assisted by careful control of the surface morphology of the PMMA and silver surface. In addition, Zhang also proved that the silver superlens can also image arbitrary nanostructures with sub-diffraction-limited resolution. The recorded image "NANO" in Fig. 3 B shows that the fine features from the mask showed in Fig. 3 A in all directions with good fidelity can be faithfully produced.

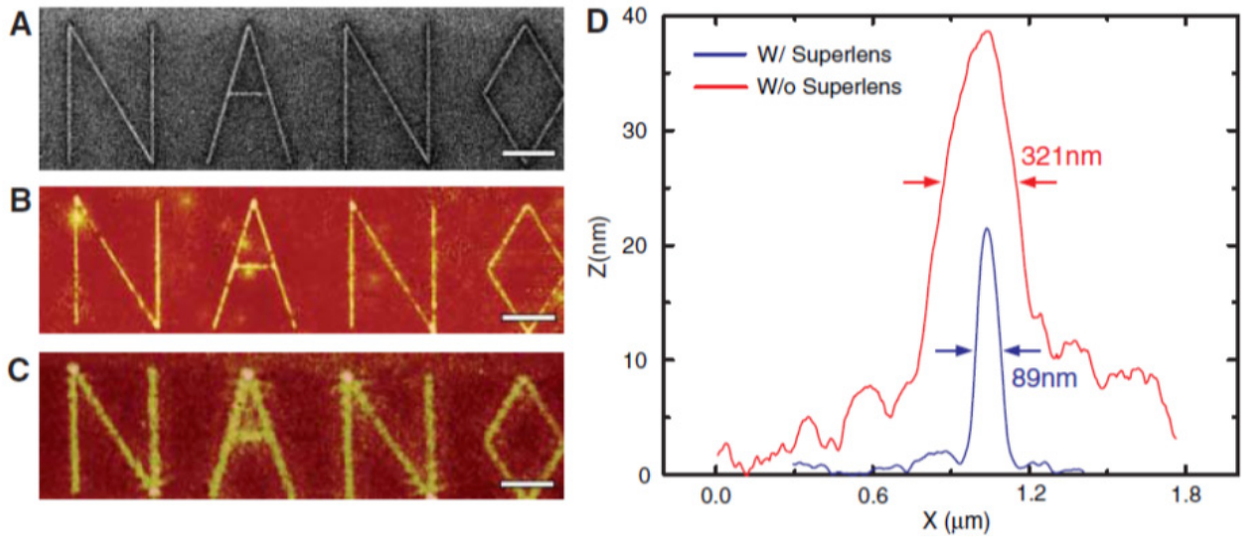

Figure 3. An arbitrary object "NANO" was imaged by silver superlens. (A) FIB image of the object. The linewidth of the "NANO" object was 40 nm. Scale bar in (A) to (C), 2 μm. (B) AFM of the developed image on photoresist with a silver superlens. (C) AFM of the developed image on photoresist when the 35 nm thick layer of silver was replaced by PMMA spacer as a control experiment. (D) The average cross section of letter "A" shows an exposed line width of 89 nm (blue line), whereas in the control experiment, we measured a diffraction-limited full width at half-maximum ling width of 321 ± 10 nm (red line). Reprinted with permission from "N. Fang, H. Lee, C. Sun and X. Zhang, Science 308, 534-537 (2005)." of copyright ©2005 American Institute of Physics.

2.2. Hyperlens

The images imaged by the superlens we talked about above are the same size as the objects. And there is no working distance. The hyperlens here was also proposed by Zhang's group [22]. It can magnify a sub-diffraction-limited image and projects it into the far field. Figure 4 A is the schematic of the hyperlens. It consists of a curved periodic stack of Ag (35 nm) and Al_2O_3 (35 nm) deposited on a half-cylindrical cavity fabricated on a quartz substrate. Sub-diffracion-limited objects were inscribed into a 50-nm-thick chrome layer located at the inner surface (air side). The anisotropic metamaterial was designed so that the radial and tangential permittivities have different signs.

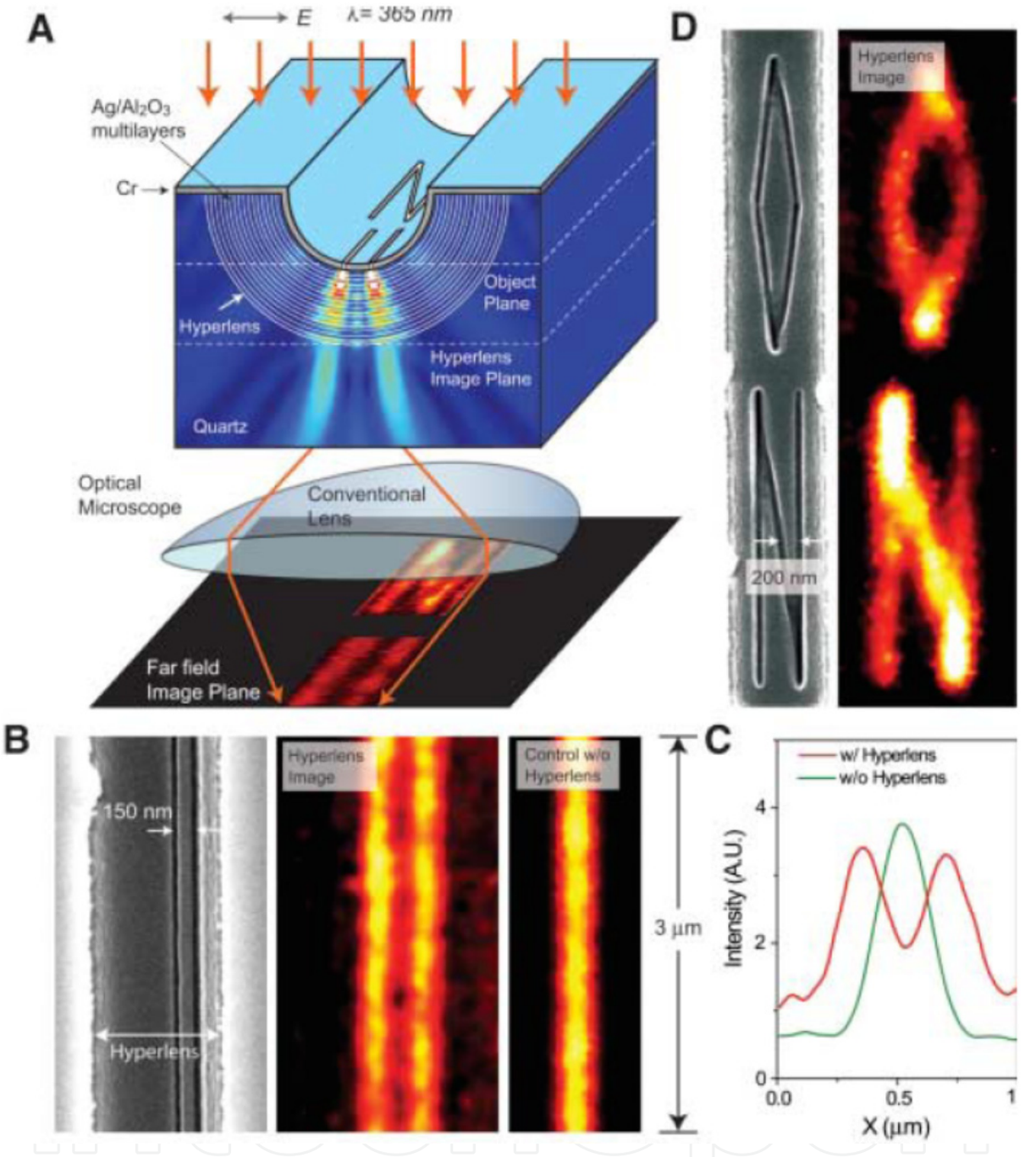

Figure 4. Optical hyperlens. (A) Schematic of heperlens and nymerical simulation of imaging of sub-diffraction-limited objects. (B) Hyperlens imaging of line pair object with line width of 35 nm and spacing of 150 nm. From left to right, scanning electron microscope image of the line pair object fabricated near the inner side of the hyperlens, magnified hyperlens image showing that the 150-nm-spaced line pair object can be clearly resolved, and the resulting diffraction-limited image from a control experiment without the hyperlens. (C) The averaged cross section of hyperlens image of the line pair object with 150-nm spacing (red), whereas a diffraction-limited image obtained in the control experiment (green). A.U.: arbitrary units. (D) An arbitrary object "ON" imaged with subdiffraction resolution. Line width of the object is about 40 nm. The hyperlens is made of 16 layers of Ag/Al_2O_3. Reprinted with permission from "Zhaowei Liu, Hyesog Lee, Yi Xiong, Cheng Sun, Xiang Zhang, Science 315. 1686 (2007)" of copyright ©2007 of AAAS.

The object imaged with hyperlens was a pair of 35-nm-wide lines spaced 150 nm apart. Upon illumination, the scattered evanescent field from the object enters the anisotropic medium and propagates along the radial direction. Because of the conservation of angular momentum, the tangential wave vectors are progressively compressed as the waves travel outward, resulting in a magnified image at the outer boundary of the hyperlens. Hence the magnified image (350-nm spacing) can be clearly resolved with an optical microscopy.

3. Plasmonic lens on the basis of subwavelength metallic structures

3.1. Subwavelength metallic structure for superfocusing

3.1.1. One-dimensional structures for focusing

In this section, we presented two types of tuning methods for the purpose of phase modulation: depth tuning [23] and width tuning [24-26] approaches.

3.1.1.1. Depth-tuned. strctures

Three types of plasmonic slits (convex, concave, and flat/constant groove depth) with different stepped grooves have been designed and fabricated to achieve efficient plasmonic focusing and focal depth modulation of the transmitted beam. Figure 5 shows the fabricated depth-tuned plasmonic lens using focused ion beam milling [27]. The general design of the plasmonic slit is shown in Fig. 6 (a) [28]. When a TM polarized (magnetic field parallel to the y-direction) monochromatic plane wave impinges on the slit, it excites collective oscillations of the electrons at the surface, which is known as SPPs. The SPPs propagate along the surface of the metal film and are diffracted to the far-field by the periodic grooves, which are designed with a width smaller than half of the incident wavelength to allow a high diffraction efficiency [29]. Constructing interference of such diffracted beams leads to the focusing effect at a certain point on the beam axis [30]. Since the diffracted beams are modulated by the nanometric grooves, through adjusting the parameters of the grooves (such as our width, depth, period and number), the diffracted beams can be fully manipulated resulting in a tailored ultra-compact lens with subwavelength resolution and nanometer accuracy [31]. Most interestingly, it has been numerically found [32] that the relative phase at the exit end of the slit increases steadily with the increasing groove depth, making it possible to achieve continuous phase retardation by simply designing surrounding grooves with stepped depths as shown in Figs. 6 (b) and 6 (c). This has led to a great simplification of the plasmonic lens design without increasing the groove number or generating a bump on the metal film [33].

Figure 7 (a) presents a detailed comparison of the measured intensity distribution with simulation using FDTD at the slit cross section (along x-direction, as indicated by the white dot line in Fig. 2 (a) [23]). A good agreement has been found between the experiment and the theoretical prediction except that the measured full-width at a half-maximum (FWHM) of the central lobe (approximately 281 nm) is slightly larger than the calculated value of about 230 nm. This is because the measured intensity distribution approximately equals to the convolution of the finite probe size (30-80nm) and the actual intensity distribution of the transmitted light.

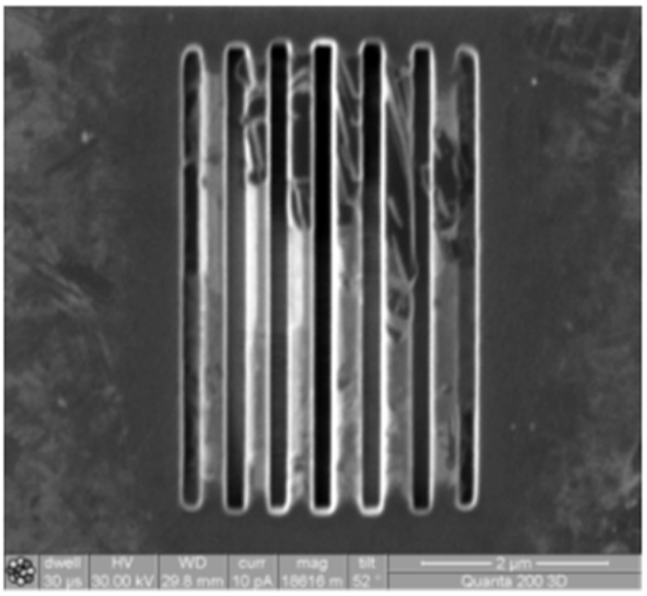

Figure 5. FIB image of the fabricated depth-tuned nanostructure (type of concave) on the Ag thin film with thickness of 200 nm.

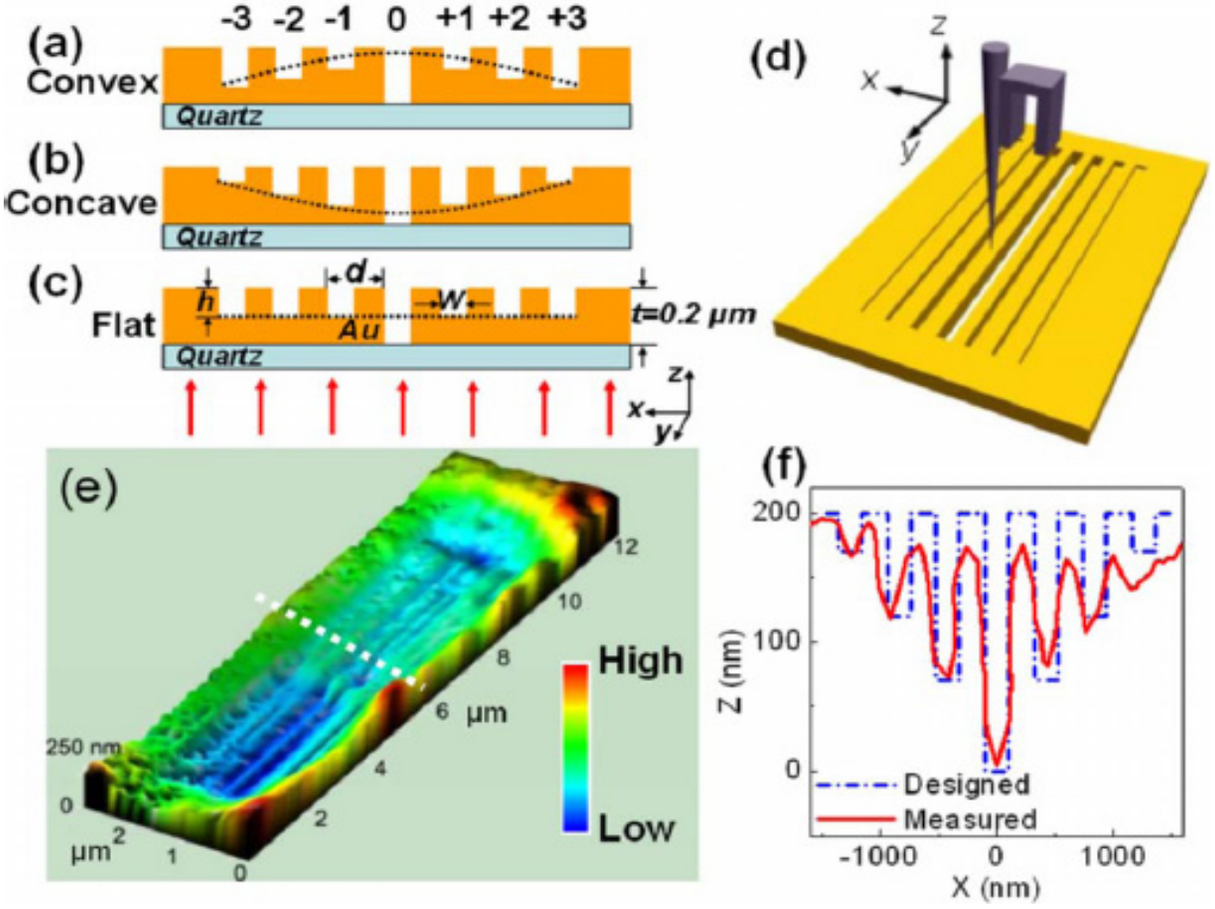

Figure 6. Schematic drawing of the nanoplasmonic slits with (a) convex, (b) concave and (c) flat shaped profiles. (d) Schematic drawing of near-field measurement setup. (e) Measured topographic image of the slit with concave corrugations. The marked area 'A' shows a larger overall depth than that of the area 'B'. (f) Cross section of the concave groove-slit at the position indicated by the dashed line in (e).

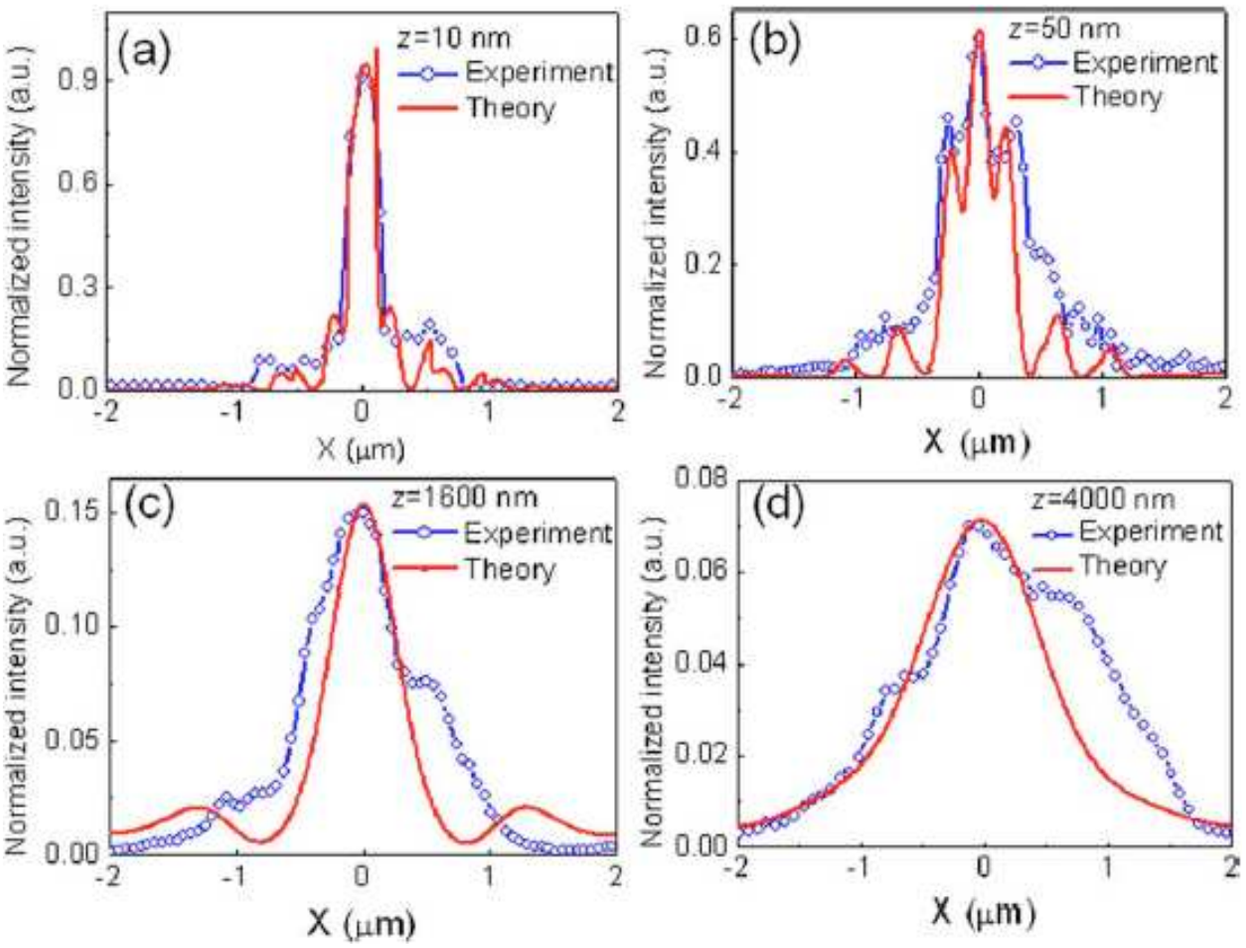

Figure 7. Comparison of measured and theoretical cross sections at x=0 in Fig. 2 of the reference paper for (a) z=10 nm, (b) z=50 nm (c) z=1600 nm and (d) z=4000 nm.

Near-field measurement reveals unambiguously the light interaction with the slits and confirms the functionalities of the nanoplasmonic lens. The simple plasmonic lens demonstrated in this paper can find broad applications in ultra-compact photonic chips particularly for biosensing and high-resolution imaging. Among the three types metallic structures, the type of convave structure has best focusing performance.

In adition, V-shaped influence on focusing performance was analyzed in fabrication point of view [34]. The incident angle dependance on the focusing properties was discussed also in Ref. [35].

Regarding fabrication of the metallic structures with depth-tuned grooves, it is worthy to point out that the geometrical characrerization issue using atomic force microscope after focused ion beam direct milling [31]. Large measurement error is found during geometrical characterization of the nanostructures by use of an atomic force microscope (AFM) working in tapping mode. Apex wearing and 34° full cone angle of the probe generate the measurement errors during characterizing the nanostructures with the feature size of 200 nm and below. To solve this problem, a FIB trimmed AFM probe is employed in the geometrical characterization, as shown in Fig. 8. The results show that the error is improved greatly using the trimmed probe.

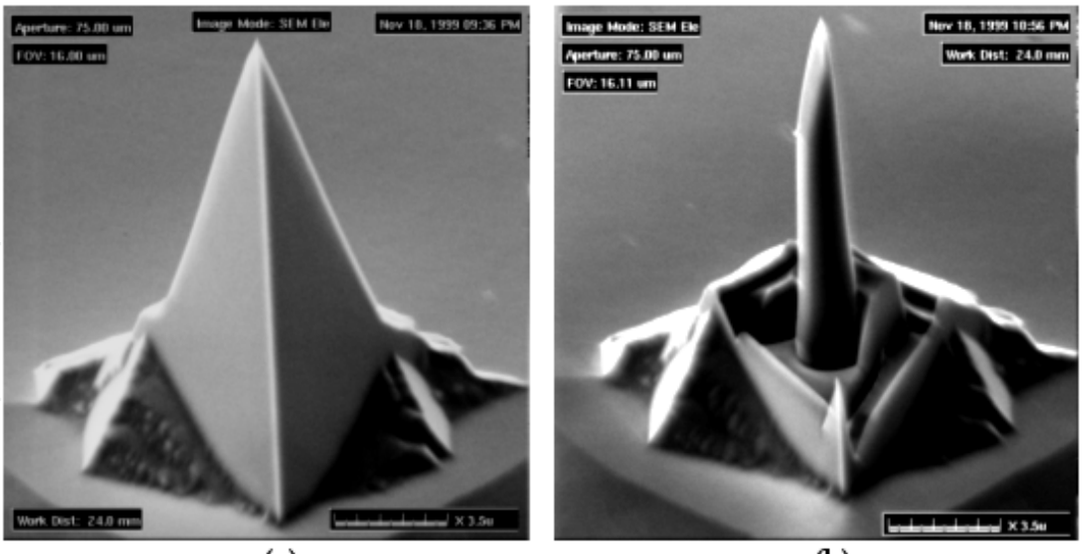

Figure 8. AFM probe for tapping mode. (a) the commercial probe with half cone angle of 17° and material of Si_3N_4. (b) the FIB trimmed probe with high aspect ratio.

Influence of polarization states on focusing properties of the depth-tuned metallic structures was reported [31]. The structure was designed with geometrical parameteres shown as Fig. 9. Figure 10 shows the total electric-field intensity $|E|^2=|Ex|^2+|Ey|^2+|Ez|^2$ at x-y plane along the longitudinal direction at z = 1.35 μm at λ=420 nm for the (a) elliptical polarization (EP), (b) circular polarization (CP), and (c) radial polarization (RP) cases. The intensity of transverse electric field, $|Ex|^2+|Ey|^2$, is significantly tuned. In the figure, the intensity along the horizontal (x) is equal to that along the vertical (y), while the intensity along the

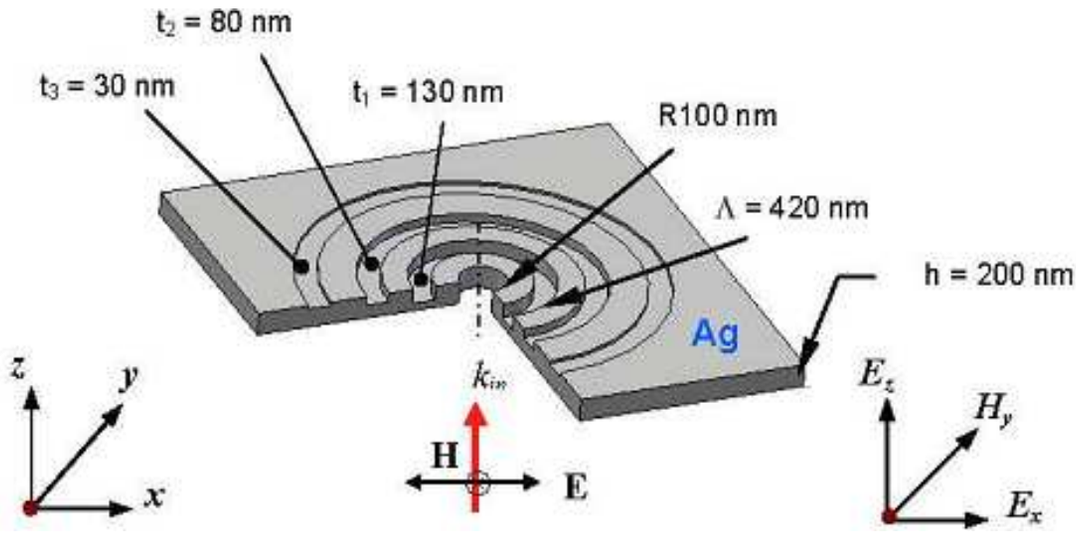

Figure 9. An annular plasmonic lens having a depth-tuned structure (groove depths, t_1= 130 nm, t_2= 80 nm and t_3=30 nm) milled in the output side of a Ag thin film (thickness, h = 200nm). Other structure parameters are: central hole diameter=200 nm, groove width=200 nm, and groove period=420 nm. The structure is incident with TM-polarized light having electric vector along the x direction. Reprinted with permission from "Jun Wang, Wei Zhou and Anand K. Asundi, Opt. Express 17, 8137-8143 (2009)." of copyright ©2009 Optical Society of American.

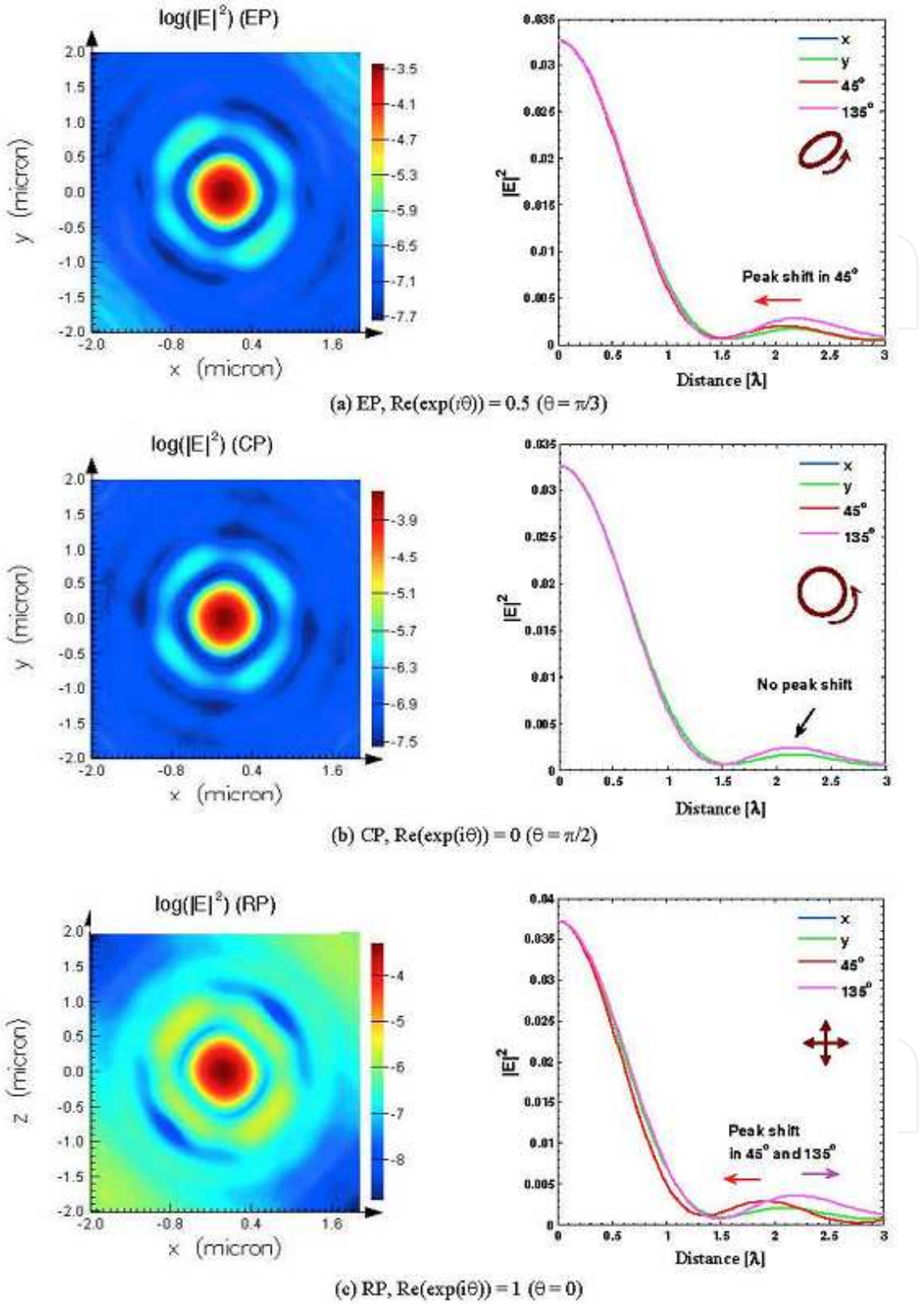

Figure 10. Total electric field (left) transmitted through the structure under illumination using different polarization states, including (a) CP, (b) EP, and (c) RP, showing the phase modulation effect on the beam profile (right) along the transverse direction in x and y and diagonal directions along 45° and 135° with respect to the x. Refer to Fig. 1 for the directions. Reprinted with permission from "Jun Wang, Wei Zhou and Anand K. Asundi, Opt. Express 17, 8137-8143 (2009)." of copyright ©2009 Optical Society of American.

diagonal directions (45° and 135° with respect to the *x* is tuned), the peak shift is observed at the side lobe, which is <0.1λ for the EP case. In Fig. 10 (a), in the direction of 45°. And the beam in 45° is narrower than that in the x- or y-directions. In addition, the phase function Re(exp(iθ)) indicates tuning capability. Re (exp(iθ)) = 0.5, where θ = π/3, for the EP case, and the phase function becomes 0 for the CP and 1 for the RP case. For example, in Fig. 10 (b), the uniformly distributed total-electric-field intensity is observed in the x-y plane, while, in Fig. 10 (c), the peak shifts 0.2λ in the 45° larger than that for the EP case, and much narrow beam is observed in the same direction. The same plasmonic modes are observed for CP, EP, or RP polarization cases as for TM case. Using a polarized plane wave the transverse electric field is tuned; the tuning 45° and 135° with respect to effect on focus spot is observed along the diagonal directions in 45° the x-direction. Of the cases, RP approach forms the smallest focus spot along the 45° using Re[exp(iθ)]=1, showing maximum tuning capability, while CP approach the phase function Re[exp(iθ)]=0 forms a symmetrically electric field distribution in the focal plane. Phase function indicates the tuning capability.

3.1.1.2. Width-tuned structures

A novel method is proposed to manipulate beam by modulating light phase through a metallic film with arrayed nano-slits, which have constant depth but variant widths. The slits transport electro-magnetic energy in the form of surface plasmon polaritons (SPPs) in nanometric waveguides and provide desired phase retardations of beam manipulating with variant phase propagation constant. Numerical simulation of an illustrative lens design example is performed through finite-difference time-domain (FDTD) method and shows agreement with theory analysis result. In addition, extraordinary optical transmission of SPPs through sub-wavelength metallic slits is observed in the simulation and helps to improve elements's energy using factor.

To illustrate the above idea of modulating phase, a metallic nano-slits lens is designed [24]. The parameters of the lens are as follows: D = 4 μm, f = 0.6 μm, λ= 0.65 μm, d=0.5 μm, where D is the diameter of the lens aperture, f the focus length, the wavelength and d the thickness of the film. The two sides of the lens is air. The schematic of lens is given in Fig. 11, where a metallic film is perforated with a great number of nano-slits with specifically designed widths and transmitted light from slits is modulated and converges in free space.

After numerous iterations of calculation using the FDTD algorithm, the resulting Poyinting vector is obtained and showed in Fig. 12 (a). A clear-cut focus appears about 0.6 micron away from the exit surface, which agrees with our design. The cross section of focus spot in x direction is given in Fig. 12 (b), indicating a full-width at half-maximum (FWHM) of 270 nm. The extraordinary light transmission effects of SPPs through sub-wavelength slits is also observed in the simulation with a transmission enhance factor of about 1.8 times. These advantages promise this method to find various potential applications in nano-scale beam shaping, integrate optics, date storage, and near-field imaging ect.

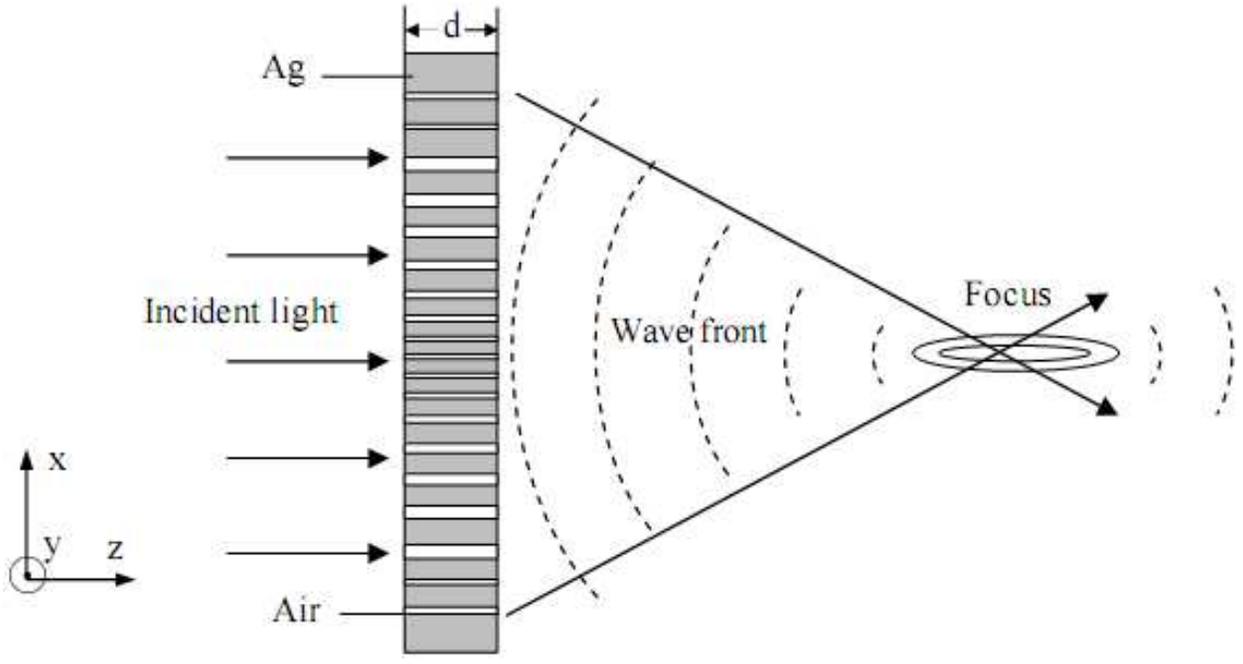

Figure 11. A schematic of a nano-slit array with different width formed on thin metallic film. Metal thickness in this configuration is *d*, and each slit width is determined for required phase distribution on the exit side, respectively. A TM-polarized plane wave (consists of Ex, Hy and Ez field component, and Hy component parallel to the y-axis) is incident to the slit array from the left side. Reprinted with permission from "H. F. Shi, C. T. Wang, C. L. Du, X. G. Luo, X. C. Dong, and H. T. Gao, Opt. Express 13, 6815-6820 (2005)." of copyright ©2009 Optical Society of American.

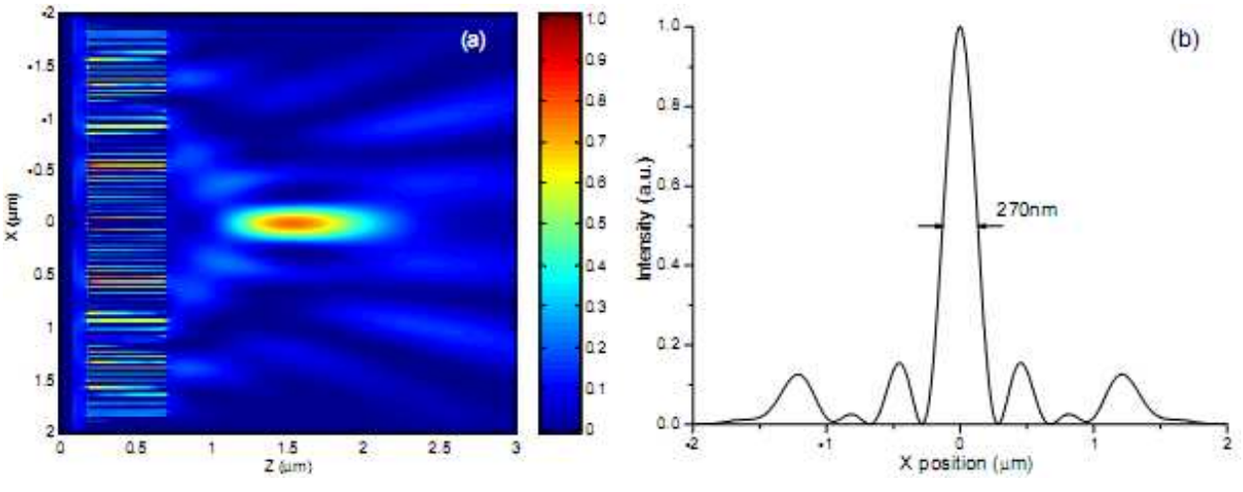

Figure 12. (a) FDTD calculated result of normalized Poynting Vector Sz for designed metallic nano-slits lens. Film thickness is 500nm, and the total slits number is 65. The structure's exit side is posited at z=0.7 μm. (b) Cross m.section of the focus at z=1.5 μm. Reprinted with permission from "H. F. Shi, C. T. Wang, C. L. Du, X. G. Luo, X. C. Dong, and H. T. Gao, Opt. Express 13, 6815-6820 (2005)." of copyright ©2009 Optical Society of American.

As an experimentlal verification example, Lieven et. al. [37] experimentally demonstrated planar lenses based on nanoscale slit arrays in a metallic film. The lens structures consist of optically thick gold films with micron-size arrays of closely spaced, nanoscale slits of varying

widths milled using a focused ion beam. They found an excellent agreement between electromagnetic simulations of the design and confocal measurements on manufactured structures. They provide guidelines for lens design and show how actual lens behavior deviates from simple theory.

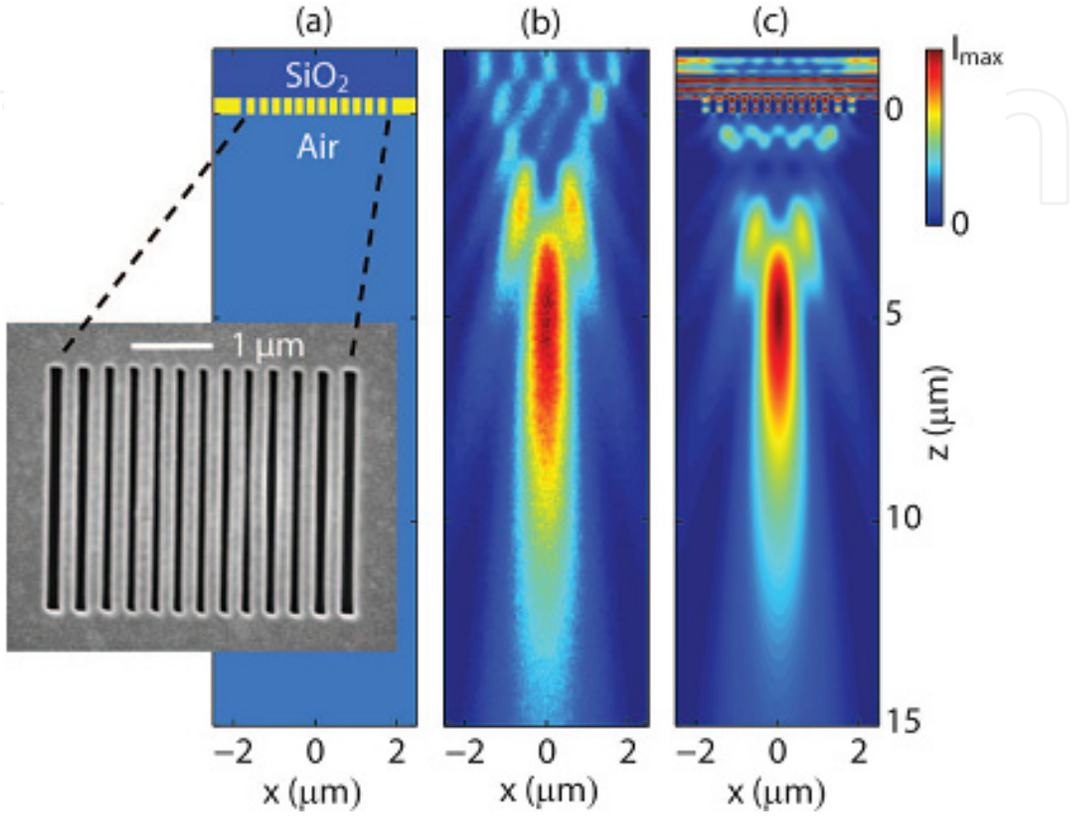

Figure 13. Planar lens based on nanoscale slit array in metallic film. (a) Geometry of the lens consisting of a 400nm optically thick gold film (yellow) with air slits of different widths (80 to150 nm) (light blue) milled therein on a fused silica substrate (dark blue). The inset shows a scanning electron micrograph of the structure as viewed from the air-side. (b) Focusing pattern measured by confocal scanning optical microscopy (CSOM). (c) Finite-difference and frequency-domain (FDFD) simulated focusing pattern of the field intensity through the center of the slits. In order to show the features of the focus spotclearly, the field intensity inside the slits is saturated. Reprinted with permission from "LievenVerslegers et. al., Nano Lett. 9, 235-238 (2009)" of copyright ©2009 Chemical Society of American.

The basic geometry consists of an array of nanoscale slits in an otherwise opaque metallic film (see Fig. 13 (a)). Figure13 shows the main results of the work, which combines fabrication, characterization, andsimulation. Pane l (a) shows the fabricated structure, while panels (b) and (c) represent the measured and simulated field intensity in across section through the center of the slits (along the x-direction). Both the measurement and the simulation clearly demonstrate focusing of the wave. The agreement between experiment and simulation is excellent. Moreover, the simulation image is generated using the designed parameters as the slit width rather than the actual slit width measured in the SEM, as is commonly done when comparing nanophotonics simulation and experiments. The agreemen there thus indicates the robustness in design and the fault tolerance of this

approach for focusing. The effect of lens size can be exploited to control the focusing behavior as is shown clearly in Fig. 14. Both lenses introduce the same curvature to the incident plane wave as the lens from Fig. 13, since we consist of slits with the same width as the original design (2.5 μm long). By omitting one outer slit on each side for the lens in Fig. 14 (a), one gets the lens, as shown in Fig. 14 (b).

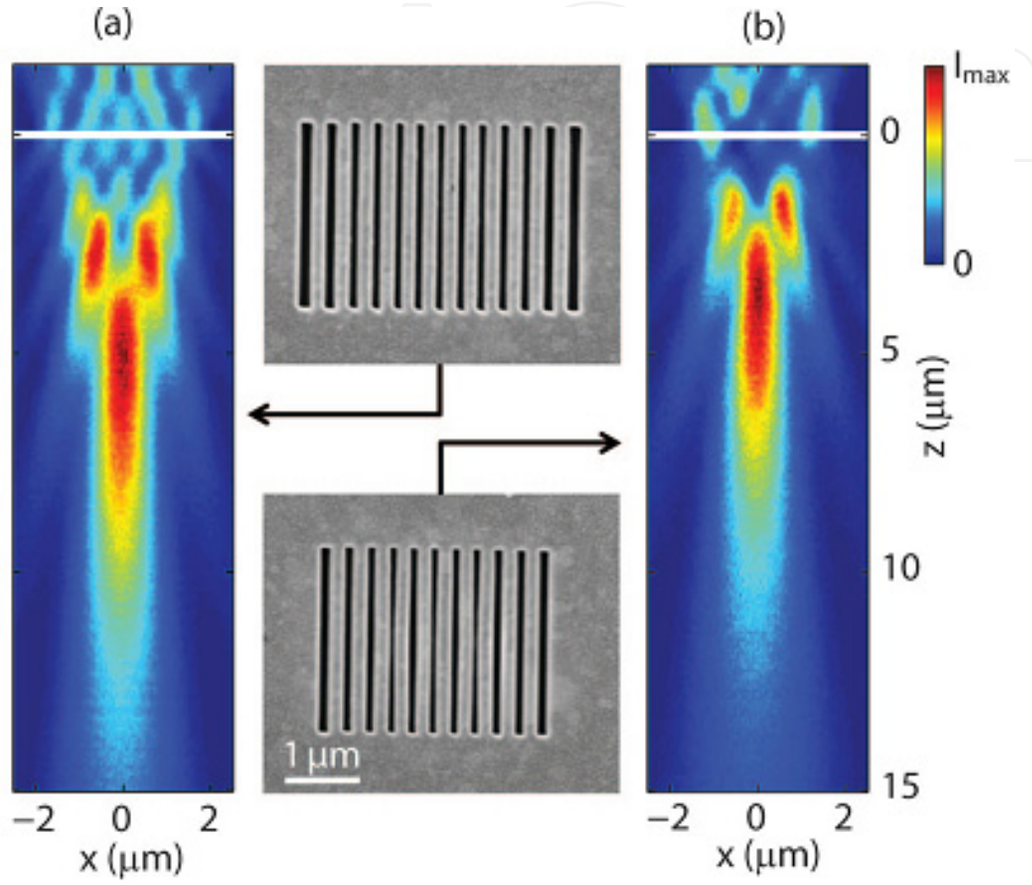

Figure 14. Control of the cylindrical lens behavior by design of nanoscale slit array parameters. Effect of lens size on focusing for (a) a lens with 13 slits (80-150nm by 2.5 μm) and (b) a lens with 11 slits (80-120nm by 2.5 μm). The white line gives an estimate of the lens position. Both scanning electron micrographs are on the same saclew. Reprinted with permission from "LievenVerslegers et. al., Nano Lett. 9, 235-238 (2009)" of copyright ©2009 Chemical Society of American.

This first experimental demonstration is a crucial step in the realization of this potentially important technology form any applications in optoelectronics. Moreover, the design principles presented here for the specil case of a lens can be applied to construct a wide range of optical components that rely on tailoring of the optical phase front.

3.1.2. Two-dimensional structures for focusing

3.1.2.1. Circular grating-based metallic structures for focusing

Recently, Jennifer et. al. reported the generation and focusing of surface plasmon polariton (SPP) waves from normally incident light on a planar circular grating (constant slits width

and period) milled into a silver film [38]. The focusing mechanism is explained by using a simple coherent interference model of SPP generation on the circular grating by the incident field. Experimental results concur well with theoretical predictions and highlight the requirement for the phase matching of SPP sources in the grating to achieve the maximum enhancement of the SPP wave at the focal point. NSOM measurements show that the plasmonic lens achieves more than a 10-fold intensity enhancement over the intensity of a single ring of the in-plane field components at the focus when the grating design is tuned to the SPP wavelength.

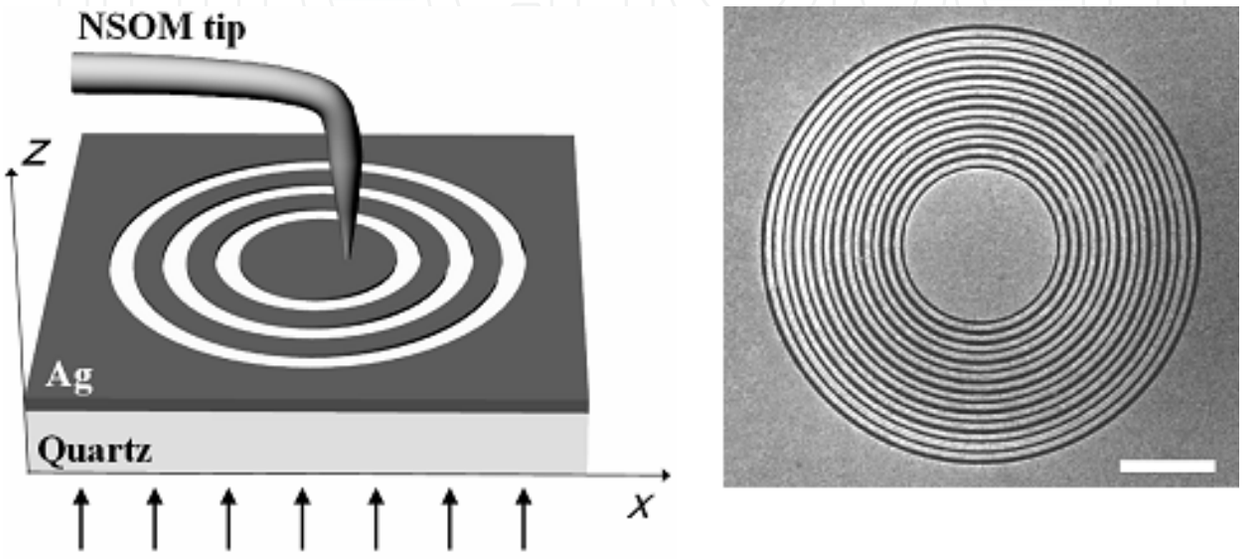

Figure 15. (a) Experimental scheme for near-field measurements. Circular gratings are cut into a silver film deposited on a quartz substrate. Laser light is normally incident from the quartz side, and the electromagnetic near-field is monitored with a metal coated NSOM tip. (b) SEM image of a sample with 15 rings. The scale bar is 5 microns. Reprinted with permission from "Jennifer M. Steele , Zhaowei Liu , Yuan Wang, and Xiang Zhang, Opt. Express 14, 5664-5670 (2006)." of copyright ©2006 Optical Society of American.

To investigate this focusing experimentally, rings with different periods were cut into 150 nm thick silver films. Silver was evaporated onto a quartz plate at a high rate to ensure a surface with minimal roughness. Rings were milled into the metal using an FEI Strata 201 XP focused ion beam (FIB), with the inner most ring having a diameter of 8 microns. Additional rings were added with a period either close to or far from resonance with the excited SPP waves. The surface plasmons were excited with linearly polarized laser light incident from the quartz side. The electromagnetic near-field of these structures was recorded using near-field scanning optical microscopy (NSOM) in collection mode using a metal coated NSOM tip. A metal coated tip was chosen over an uncoated tip to increase the resolution of the scan. Previous experimental results on samples with similar geometry compare favorably with computer simulations, indicating the interaction of the SPP near field with the metal tip is negligible. The measurement scheme can be seen in Fig. 15 (a) with an SEM image of a typical sample shown in Fig. 15 (b). The phase change of SPP waves across a barrier is an interesting issue that has received very little attention. If the slit width

is much smaller than the SPP wavelength, the slit will have very little effect on the SPP and the phase change should be very small. However, if the slit width is on the order of the SPP wavelength, as the SPP waves cross a slit opposite charges will be induced on opposite sides of the slit, providing quasi-electrostatic coupling across the barrier. The authors calimed that it is possible that the phase change will be sensitive to the slit width. The number and period of rings, film material, and slit geometries provide experimental handles to tune the plasmonic lens to accommodate specific applications, making this technique a flexible plasmonic tool for sensing applications.

The following two sections below introduce the metallic subwavelength structures with chirped (variant periods) slits and nanopinholes acted as the plasmonic lenses for the purpose of superfocusing.

3.1.2.2. Illumination under linear polarization state

A novel structure called plasmonic micro-zone plate-like (PMZP) or plasmonic lens with chirped slits is put forth to realize superfocusing. It was proposed by Fu's group [39,40]. Unlike conventional Fresnel zone plate (CFZP), a plasmonic structure was used and combined with a CFZP. Configuration of the PMZP is an asymmetric structure with variant periods in which a thin film of Ag is sandwiched between air and glass. The PMZP is a device that a quartz substrate coated with Ag thin film which is embedded with a zone plate structure with the zone number N < 10. Figure 16 is an example of schematic diagram of the structure.

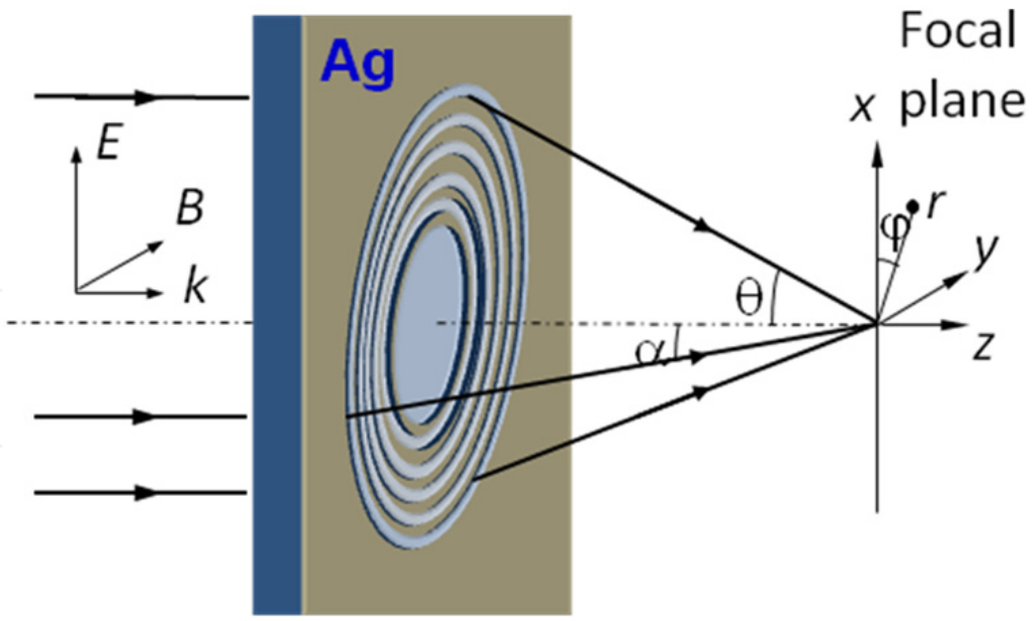

Figure 16. Schematic of the plasmonic micro-zone plate for super-focusing.

Following the electromagnetic focusing theory of Richard and Wolf (Richards & Wolf, 1959)[41], the electric field vector in the focal region is given by,

$$\mathbf{E}(r, z, \varphi) = -i\,[I_0(r, z) + I_2(r, z)\cos 2\varphi\,]\,\mathbf{i} - i\,I_2(r, z)\sin 2\varphi\,\mathbf{j} - 2I_1(r, z)\cos\varphi\,\mathbf{k}. \quad (2)$$

Let **i**, **j**, **k** be the unit vectors in the direction of the co-ordinate axes. To be integral over the individual zones, I_0, I_1, I_2 are expressed as,

$$I_0(r,z) = \sum_n T_n \int_{\alpha_{n-1}}^{\alpha_n} \sqrt{\cos\theta}\,(1+\cos\theta) J_0(kr\sin\theta)\exp(ikz\cos\theta)\sin\theta d\theta,$$

$$I_1(r,z) = \sum_n T_n \int_{\alpha_{n-1}}^{\alpha_n} \sqrt{\cos\theta}\sin\theta J_1(kr\sin\theta)\exp(ikz\cos\theta)\sin\theta d\theta,$$

$$I_2(r,z) = \sum_n T_n \int_{\alpha_{n-1}}^{\alpha_n} \sqrt{\cos\theta}\,(1-\cos\theta) J_2(kr\sin\theta)\exp(ikz\cos\theta)\sin\theta d\theta.$$

The wave vector $k = 2\pi/\lambda$.

According to the equation, the intensity of lateral electric field component, $|E_x|^2$, follows the zero-order Bessel function J_0 of the first kind, while the intensity of longitudinal electric field component, $|E_z|^2$, follows the first-order Bessel function J_1 of the first kind. In the total electric field intensity distribution, all the field components add up. With high numerical aperture, this leads to not only asymmetry of the focus spot but also an enlarged focus spot. As shown in Figs. 17 (a)~(b), the total electric field and individual electric field components, $|E|^2$, $|E_x|^2$, &$|E_z|^2$, emerged from λ_{sp}-launched FZP lens are in comparison with that the total electric field and individual electric field components from a λ_{in}-launched PMZP lens. It is found that the intensity ratio, $|E_x|^2/|E_z|^2$, can increase up to 10 times for the λsp-launched PMZP lens. A focus spot having the polarization direction along the x direction is obtained.

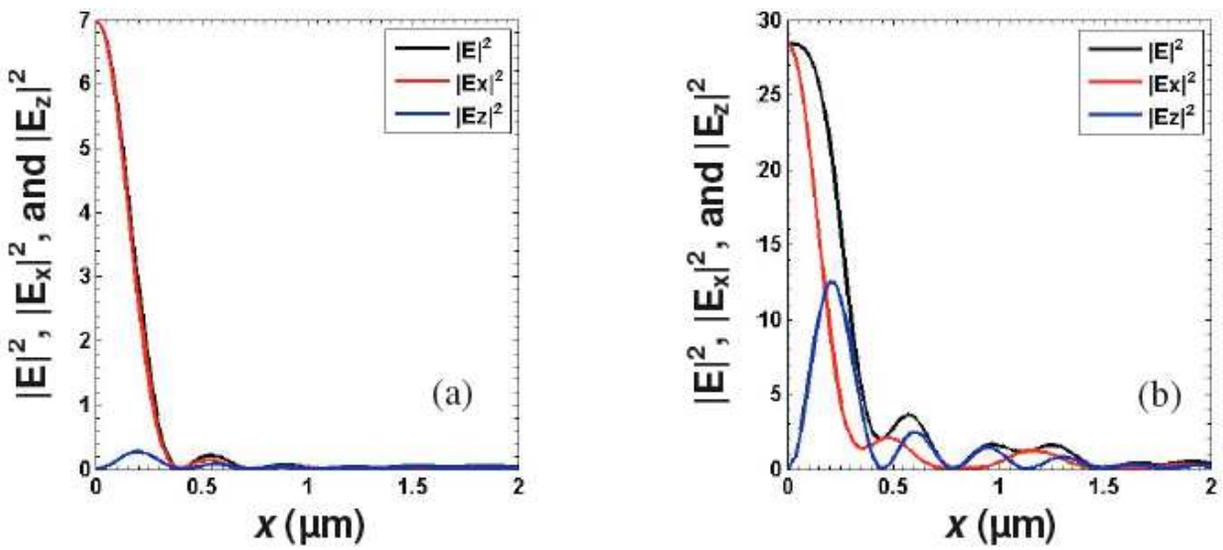

Figure 17. The total electric field and electric field components, $|E|^2$, $|E_x|^2$, and $|E_z|^2$, emerged from (a) a λ_{sp}-launched FZP lens and (b) a λ_{in}-launched FZP lens. It is observed that the proposed superlens enables to restrict the depolarization effect and produces a linearly- polarized focus spot having the polarization direction in the *x* direction.

The chirped slits can form a focal region in free space after the exit plane. The final intensity at the focal point is synthesized by iteration of each zone focusing and interference each other, and can be expressed as

$$I = \alpha \sum_{i=1}^{N} C I_0 \frac{4r_i}{\lambda_{SP}} e^{-(r_i / l_{SP})} \tag{3}$$

where I_0 is the incident intensity, r_i is the inner radius of each zone, i is the number of the zones, l_{SP} is the propagation length for the SPP wave, α is interference factor, and C is the coupling efficiency of the slits. C is a complicated function of the slit geometry and will likely have a different functional form when the slit width is much larger or much smaller than the incident wavelength

The PMZPs is an asymmetric structure. For an evanescent wave with given k_x, we have $k_{zj} = +[\varepsilon_j(\omega/c)^2 - k_x^2]^{1/2}$ for j=1 (air) and j=3 (glass) and $k_{zj} = +i[k_x^2 - \varepsilon_j(\omega/c)^2]^{1/2}$ for j=2 (Ag film). Superfocusing requires regenerating the evanescent waves. Thus the PMZP needs to be operated with the condition $|k_{z1}/\varepsilon_1 + k_{z2}/\varepsilon_2||k_{z2}/\varepsilon_2 + k_{z3}/\varepsilon_3| \to 0$. Physically, this would require exciting a surface plasmon at either the air or the glass side. For $E_\perp$ wave, a negative permittivity is sufficient for focusing evanescent waves if the metal film thickness and object are much smaller than the incident wavelength. Because electric permittivity $\varepsilon < 0$ occurs naturally in silver and other noble metals at visible wavelengths, a thin metallic film can act as an optical super lens. In the electrostatic limit, the p-polarized light, dependence on permeability μ is eliminated and only permittivity ε is relevant. In addition, diffraction and interference contribute to the transition from the evanescent waves to the propagation waves in the quasi-far-field region. Above all, the PMZPs form super focusing by interference of the localized SPP wave which is excited from the zones. This makes it possibly work at near and quasi-far-field with lateral resolution beyond diffraction limit. Also the PMZP has several zones only, its dimension is decreased greatly compared the CFZP.

As an example, an appropriate numerical computational analysis of a PMZP structure's electromagnetic field is carried out using finite-difference and time-damain (FDTD). It is illuminated by a plane wave with a 633 nm incident where Ag film has permittivity $\varepsilon_m = \varepsilon_m^{'} + i\varepsilon_m^{''} = -17.6235 + 0.4204i$. An Ag film with thickness $h_{Ag} = 300nm$ centered at z=150 nm has an embedded micro-zone-plate structure. Zone number N=8, and outer diameter OD=11.93 μm. The widths of each zone from first ring to last ring, calculated by using the conventional zone plate equations, are 245, 155, 116, 93, 78, 67, 59, and 52 nm. In the FDTD simulations, the perfectly

matched layer boundary condition was applied at the grid boundaries. Figure 17 is the simulation result. From the result, the simulated focal length of the PMZP, f_{PMZP} and depth of focus (DOF) are larger than those of the designed values using the classical equations $r_n = (n\lambda f_{FZP} + n^2\lambda^2/4)^{1/2}$ and $DOF = \pm 2\Delta r^2/\lambda$, where n=1, 2, 3,…, f_{PMZP} is the designed principal focal length of Fresnel zone plates and given in terms of radius R of the inner ring